Heliyon 10 (2024) e34880

Contents lists available at ScienceDirect

Heliyon

journal homepage: www.cell.com/heliyon

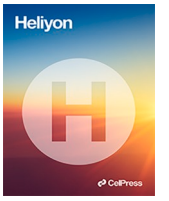

Research article

Unveiling the potential of NiO–$ZnCo_2O_4$ nano-composites: Electrical, optical, electrochemical and antibacterial investigation

Adiba Adiba [a,*], Mo Ahamad Khan [b], Tufail Ahmad [a]

[a] Department of Physics, Aligarh Muslim University, Aligarh, 202002, India
[b] Department of Microbiology, Faculty of Medicine, Aligarh Muslim University, Aligarh, 202002, India

ARTICLE INFO

Keywords:
NiO
$ZnCo_2O_4$
Supercapacitor
Anti-bacterial
Wide band gap

ABSTRACT

Zinc Cobaltite (ZCO) and Nickel Oxide (NiO) nanoparticles (NPs) were synthesized using a sol-gel technique, and their composites with different weight ratios were prepared using a straightforward sonication method. The NiO and ZCO NPs had small crystallite size of 10 nm and 18 nm, respectively. According to the ultraviolet–visible (UV–Vis) spectra, pure NiO and ZCO NPs exhibited band gaps of ~3.5 eV and 3.3 eV. Antibacterial activity against gram-positive (*Staphylococcus aureus*) and gram-negative (*Escherichia coli*) bacterial strains was also tested for the composite counterpart and its equivalents. Compared to pure NPs, the composite of 30 % ZCO-NiO (NZ3) had higher antibacterial activity with zone of inhibition of ~13 mm against *E. coli*. The electrical and electrochemical properties were also explored and it was found that the composite of 50 % ZCO-NiO (NZ5) shows high specific capacitance of 188 F/g.

1. Introduction

In the face of mounting concerns over the finite supply of fossil fuels, environmental sustainability, and the need for cleaner energy sources, the quest for efficient and eco-friendly energy solutions has never been more crucial. This imperative has sparked a surge of interest in renewable energy alternatives, like solar, tidal, and wind power, as well as the development of advanced energy storage technologies to harness and utilize these intermittent energy sources. Among these storage solutions, supercapacitors have garnered substantial attention for their high-power density, extended cyclic stability, and rapid recharge capabilities [1]. Various transition metal oxides, spinels, carbon-based materials, etc. have been considered as candidates for supercapacitors. Among them, NiO, a p-type semiconductor having visible light transparency with a wide band gap, is acknowledged for its high theoretical capacitance. Moreover, it finds utility in diverse fields, including energy production and storage, memory devices, antimicrobial films, and gas sensors [2–6]. However, low conductivity of NiO nanoparticles (NPs) limits its performance as a supercapacitor which can be enhanced by employing strategies such as nano-composite formation, doping, and surface modification [7–9]. $ZnCo_2O_4$ (ZCO) with high conductivity and structural stability may synergistically work with NiO to result in high electrochemical activity [10–12].

Concurrently, in the realm of healthcare, the surge in antibiotic-resistant bacterial infections has spurred the search for novel antibacterial interventions [13,14]. The rapid rise of antibacterial resistance outpacing the speed at which new antibiotics are being discovered, poses a significant challenge in healthcare. However, innovative approaches such as the utilization of nanoparticles directly as antibiotics, for targeted drug delivery and magnetic hyperthermia etc. are being researched as a potential solution [15–19].

* Corresponding author. Department of Physics, Aligarh Muslim University, Aligarh, 202002, Uttar Pradesh, India.
E-mail addresses: adibaeshaal@gmail.com (A. Adiba), ahmadk065@gmail.com (M.A. Khan), tufailahmadphys@gmail.com (T. Ahmad).

https://doi.org/10.1016/j.heliyon.2024.e34880
Received 26 December 2023; Received in revised form 3 July 2024; Accepted 18 July 2024
Available online 18 July 2024

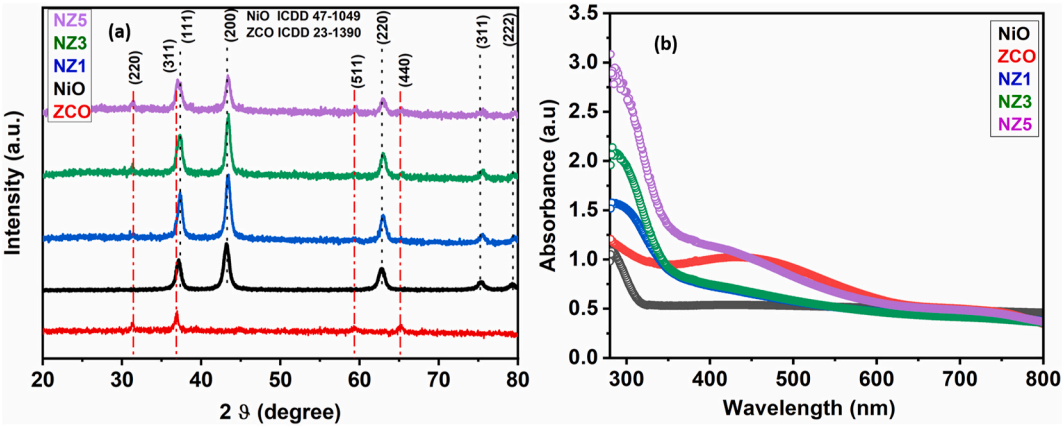

Fig. 1. (a) XRD spectra (b) Absorbance spectra of bare NiO, $ZnCo_2O_4$, and NiO– $ZnCo_2O_4$ composites.

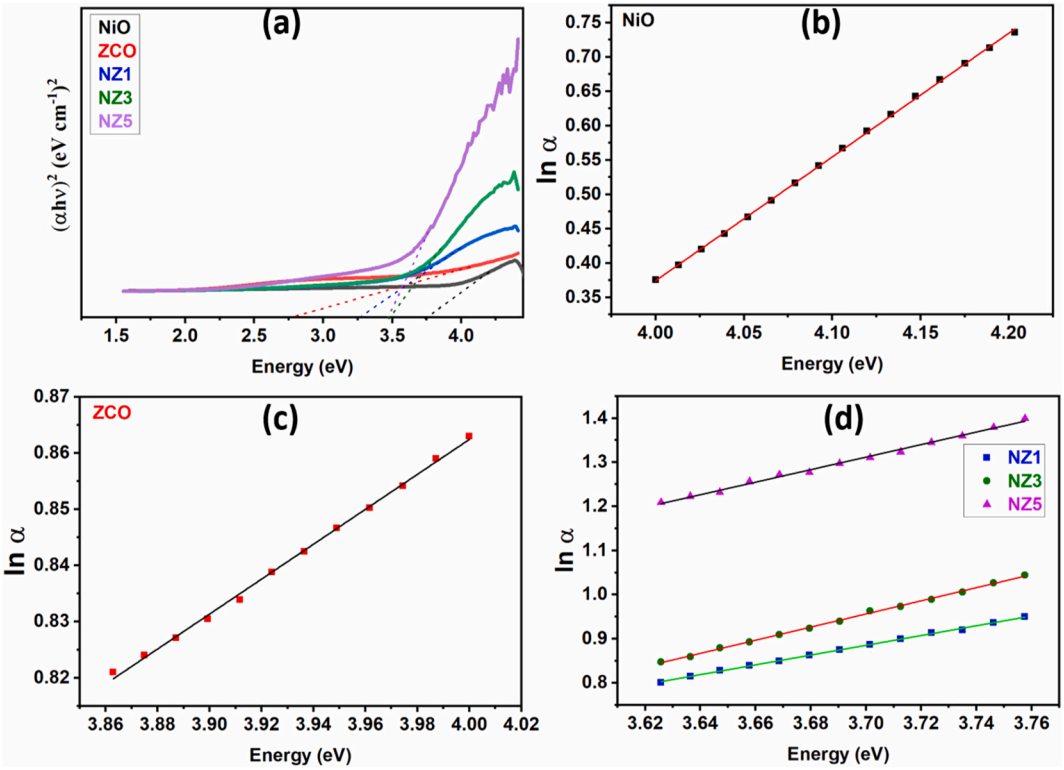

Fig. 2. (a) Tauc Plot (b)–(d) Arrhenius Plot of bare NiO, $ZnCo_2O_4$, and NiO–$ZnCo_2O_4$ composites.

Using nanoparticles to achieve antibacterial potency is one step towards the future where medicine could be revolutionized by the integration of nanoparticles and genetic-based therapies. Nanomaterials, particularly transition metal oxide like ZnO, NiO, and CuO_2, are being considered due to their potential antibacterial efficacy, cost-effectiveness, and abundance [13,14,20].

Recognizing these existing challenges and the potential synergy between the properties of ZCO and NiO, this study centres on the synthesis of NiO-ZCO composite nanostructures at varying concentrations. Specifically, the focus lies in synthesizing and exploring the optical, electrical, antibacterial, and electrochemical activities of NiO-ZCO nanostructures. Remarkably, our investigations revealed the growth-inhibitory and antibacterial activities of the NiO-ZCO composites against pathogenic bacteria, particularly *E. coli* and *S. aureus*, signalling potential applications in transparent antimicrobial coatings for diverse purposes, such as glass windows, walls and beds of operation theatres and labour rooms, and on medical and surgical instruments and implants. Moreover, the NiO-ZCO composites also showed enhanced specific capacitance suggesting their potential to serve as an effective material for supercapacitor electrodes.

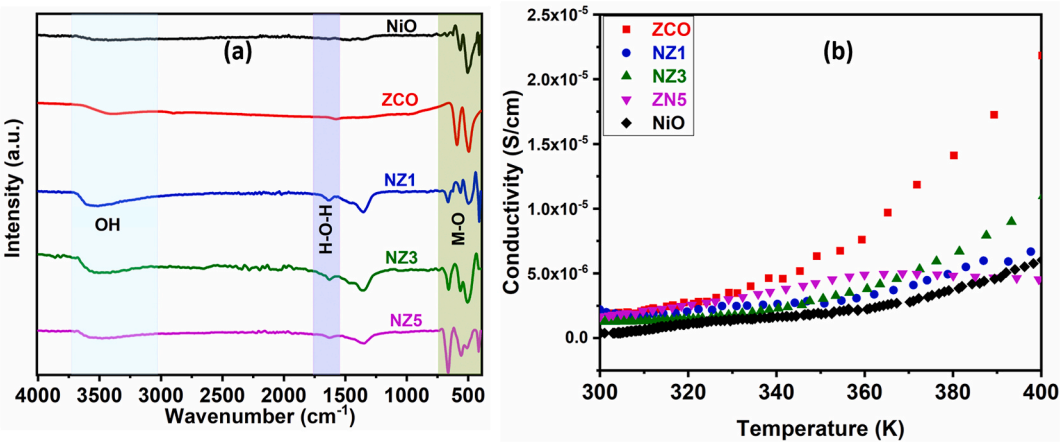

Fig. 3. (a) Spectral mapping via FTIR (b) DC conductivity of bare NiO, $ZnCo_2O_4$ and NiO–$ZnCo_2O_4$ composites.

2. Experimental

The information can be found in the Supplementary file.

3. Results and discussion

3.1. Characterization of the samples

Fig. 1a shows the XRD pattern of the synthesized samples. The peaks marked in black are in agreement with JCPDS 47–1049 showing successful synthesis of NiO nanoparticles with space group $fm\bar{3}m$ and a face-centered cubic crystal structure [21–23]. The peaks in red are for spinel $ZnCo_2O_4$ nanoparticles (JCPDS 23–1390), showing a tetragonal structure with $fd\bar{3}m$ [24]. No extra peaks could be seen in the XRD pattern for the NiO–$ZnCo_2O_4$ composite. The peaks could be discerned for both the 30 % and 50 % ZCO-NiO (here onwards referred as NZ3 and NZ5) samples easily however for the 10 % ZCO composite sample (NZ1), the intensity of the peak is much less, amounting to a lesser percentage of ZCO as compared to NiO. There is no change in peak position after composite formation indicating that $ZnCo_2O_4$ did not integrate into NiO lattice [25]. The size of crystallites (D_{hkl}) was assessed through the application of Scherrer's formula.

$$D_{hkl} = \frac{K\lambda}{\beta_{hkl} \times \cos\theta} \tag{1}$$

where K = 0.9 is the factor accounting for crystallite shape, β_{hkl} is the full width at half-maximum, λ stands for the X-ray wavelength of Kα radiation, and θ is the Bragg angle [26]. The determined D_{hkl} for NiO, $ZnCo_2O_4$, NZ1, NZ3, and NZ5 are ~10.5, 18.2, 16.2, 14.8 and 15.3 nm, respectively.

As illustrated in Fig. 1b, UV–visible spectroscopy was conducted to uncover the optical characteristics of the materials. The band gap energy was determined using Tauc plot analysis (Fig. 2a). This estimation was done using Kubelka-Munk function (α) in the equation:

$$[\alpha h\nu]^n = A(h\nu - E_g) \tag{2}$$

Where ν represents frequency of light, h is Planck's constant, n is ½ for indirect allowed and 2 for direct allowed transitions, A is a constant, and E_g is the band gap [27,28]. NiO is known to be a wide band gap semiconductor, and we obtained a value of 3.52 eV in accordance with our previous reports. For $ZnCo_2O_4$, we got a value of 3.32 eV that agrees with the reported values [29,30]. Stoica et al. reported a band gap of around 3.72 eV and concluded that the valence band is significantly influenced by O 2p orbitals, with a deep valence hybridization with the Zn 3d orbitals and substantial shallow hybridization with Co 3d orbitals [31]. For the composite samples, the band gap values are 3.29 eV, 3.40 eV, and 3.46 eV for NZ1, NZ3, and NZ5, respectively. For transition metal oxides, it has also been observed that band gap is size dependent and increases with decrease in crystallite size [32,33]. Moreover, the band gap value is also affected by emergence of new energy states for composites [34]. Hence, the observed trend in band gap variation may be explained by combined effect of new energy states and the increased crystallite size that cause shifting of absorption bands towards lower wavelength.

The absorption coefficient (α) is known to exhibit exponential behaviour concerning photon energy near the band edge, typically referred to as the Urbach region (hυ < Eg):

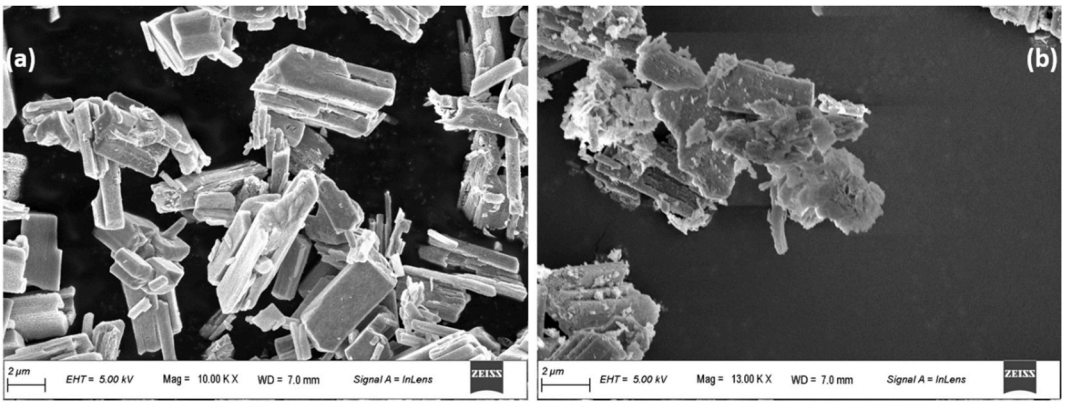

Fig. 4. Sem image of (a) ZCO (b) NiO–$ZnCo_2O_4$ composites.

$$\alpha \sim \exp\left(\frac{h\upsilon}{E_u}\right) \tag{3}$$

Here, E_u denotes the Urbach energy, and α is the absorption coefficient. E_u signifies the width of the band tails associated with localized states accounting for transitions between localized and extended states within the conduction band and provides insight into structural irregularities within materials, leading to indirect assessment of defect concentrations in nanomaterials. We have determined the Urbach value by analysing the slope of the linear part of the plot (ln α vs hυ) as depicted in Fig. 2(b–d). The resulting E_u values are 0.55 eV for pure NiO, 3.21 eV for ZCO, 0.90 eV for NZ1, 0.67 eV for NZ3, and 0.70 eV for NZ5. Notably, the E_u values display irregular increase in the composites. This could be attributed to the emergence of various imperfections in the crystal lattice, leading to the creation of additional localized levels within the bandgaps.

The FT-IR spectra of the individual sample along with the composites are shown in Fig. 3a. The strong peak seen at 400 cm^{-1} for pure NiO can be ascribed to the metal-oxygen bond stretching, specifically the Ni–O stretching mode [23,35]. In the $ZnCo_2O_4$ spectra, bands around 570 cm^{-1} and 670 cm^{-1} are allotted to Co–O and Zn–O vibrations, respectively [24]. In general, the vibrational frequency is determined by atomic weight of metallic ions as well as the bond length between the octahedral and tetrahedral sites. The varied vibrational frequencies in the zinc cobaltite spinel structure are caused by this variation in bond length [36,37]. We can see broad curves between 1550 and 1750 cm^{-1} and 3000-3800 $cm^{-1,}$ which can be allocated to bending and stretching mode of water [38, 39]. These two modes demonstrate the adsorbed water on the NPs' surface. The formation of composite is implied by the distinctive peaks of NiO and $ZnCo_2O_4$ in the spectra.

SEM images were used to examine the morphology and microstructure of ZCO and NiO-ZCO composite, as shown in Fig. 4 a,b. The ZCO nanoparticles exhibit a distinctive nanorod morphology, characterized by elongated structures with well-defined facets. The nanocomposite reveals the incorporation of NiO nanoflakes, which intercalate among the ZCO nanorods. The nanorod-shaped ZCO may provide high aspect ratios, facilitating efficient charge transport pathways, while the NiO nanoflakes likely contribute to increased surface area, which synergistically results in higher electrochemical activity as seen in the later section. The elemental composition of the ZCO and NiO-ZCO composite, as determined by energy dispersive X-ray analysis (EDX), is shown in Figs. S2 and S3 (SI). It was confirmed that Zn, Co, Ni, and O were present in the composite.

3.2. Electrical properties

The variation of DC conductivity with temperature for both the individual sample and the composites with varying ZCO content is shown in Fig. 3b. All the samples demonstrate negative temperature coefficients of resistance; this increase in conductivity with the rise in temperature reveals their semiconducting nature. Arrhenius type dc conductivity is expressed for all the samples except for the NZ5 sample, which is a weak function of temperature above 358 K. The most plausible reason for p type conductivity in NiO is the charge compensation of the Nickel vacancies. The understanding of nature of this electronic compensation is tricky with localized charges forming either on nickel or oxygen atoms. Poulain et al. studied the role of deposition temperature for sputtered NiO thin films and concluded that this charge compensation is enabled by peroxo-species and free holes [40]. A DC conductivity of order 10^{-7} Scm^{-1} is achieved at room temperature for both NiO and ZCO, which is comparable to the reported values. The interaction between Co 3d electrons (with tetrahedral coordination) and the O 2p electrons significantly impacts the electrical properties in ZCO, while Zn atom (with octahedral coordination) is comparatively passive in deciding the valence electronic properties for the zinc cobaltite spinel structure [31].

The conductivity of the composite is determined by the accumulation of excess charges at the interface along with the intra-grain defects at the boundary [41]. As the temperature increases, the electrons attain enough energy to overcome the potential barrier and hop between the sites. The number of charge carriers may potentially increase with increasing amount of ZCO; therefore, a trend of increasing conductivity is observed. However, the low conductivity of the NZ5 sample can be explained by a large number of

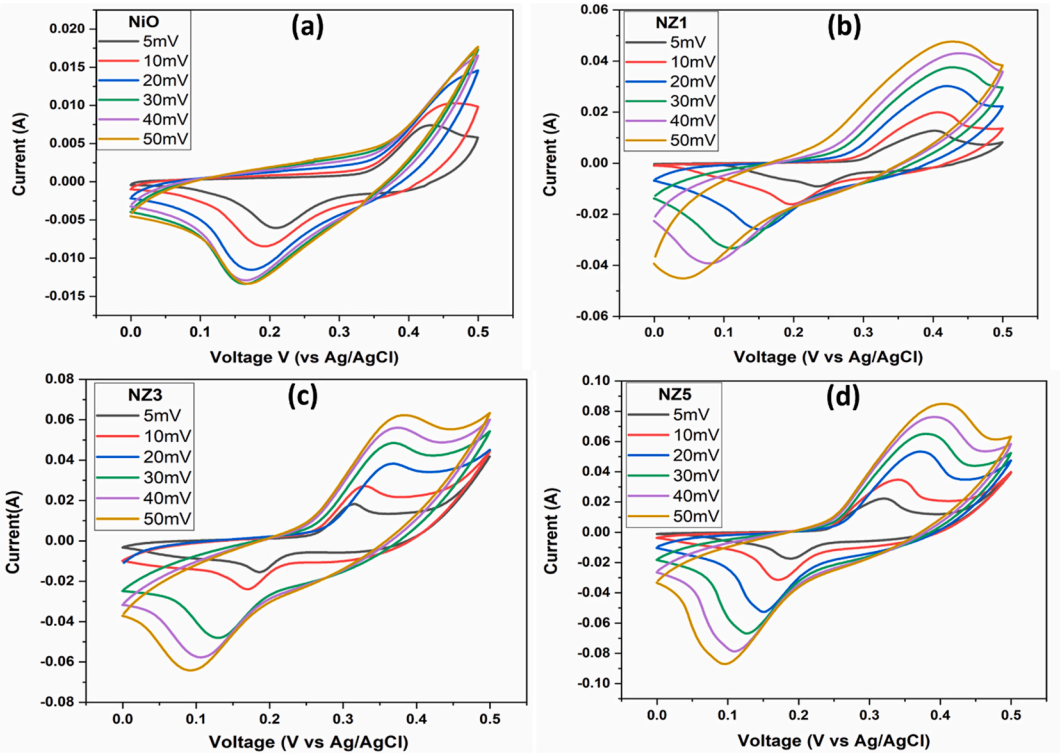

Fig. 5. (a–d) CV of bare NiO and NiO–$ZnCo_2O_4$ nano-composite.

intra-grain defects due to the increased concentration of the component, along with the presence of agglomerated particles.

When we fit the experimental data to the Arrhenius thermally activated equation given as:

$$\sigma = \sigma_0 \left(e^{\frac{-\Delta E}{KT}} \right) \tag{4}$$

we find a good linear fit. The relationship between the natural logarithm of σ and the reciprocal of temperature (expressed as 1000/T) displays nonlinear behaviour across the entire temperature range for all the samples, as can be seen from Fig. S1 (SI). This nonlinearity observed in the data confirms that multiple thermally activated processes contribute to these samples' conductivity. Our primary objective is to determine the activation energy by examining the slope of the linear portion of the Arrhenius plot, specifically within the lower temperature range of 294–344 K. The calculated activation energy values for all the samples in this temperature range fall within the 200–400 meV range. The value of the activation energy points towards hopping between the nearest neighbouring sites [42–44].

3.3. Electrochemical performance

Fig. 5 illustrates the cyclic voltammetry (CV) plots of various electrodes within 0.0–0.5 V (versus Ag/AgCl) at scan rates ranging from 5 mV/s to 50 mV/s. All of these electrodes exhibit clear redox peaks resulting from Faraday oxidation-reduction reactions, indicating that they possess characteristics similar to those of battery-type electrode materials [45]. For NiO, the peaks occur at ~0.15 V and 0.42 V which can be attributed to faradaic redox reactions [46]. For the NiO-ZCO composite samples, the presence of reversible faradaic reactions in the curves is associated with A–O and A–O–OH, where A can be Zn, Co or Ni [47]. The redox reaction can be written as:

$$ZnCo_2O_4 + H_2O + OH^- \rightarrow ZnOOH + 2CoOOH + e^- \tag{5}$$

$$CoOOH + OH^- \rightarrow CoO_2 + H_2O + e^- \tag{6}$$

$$NiO + OH^- \rightarrow NiOOH + e^- \tag{7}$$

The composite electrodes show a superior response in terms of current and feature larger enclosed areas within the CV curves when compared to the individual sample. This observation reveals the exceptional charge storage capacity of the composite electrodes.

Notably, the NZ5 electrode displays the highest current and the largest enclosed CV curve area, highlighting the influence of the composite's composition and proportions on the electrochemical efficiency of the electrodes.

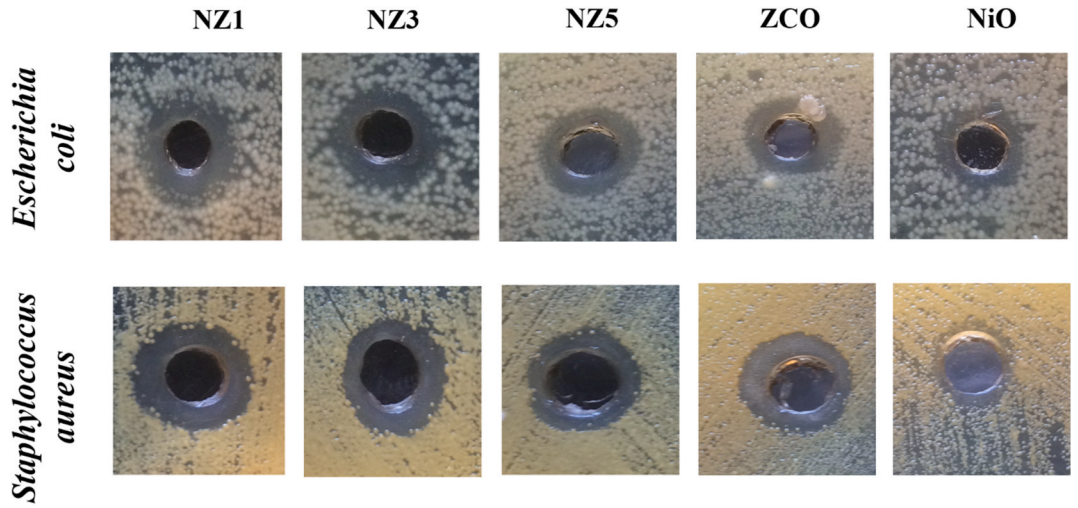

Fig. 6. Antibacterial efficiency shown by Zone of Inhibition using NiO, ZCO and the composites.

Table 1
Zone of Inhibition using NiO, ZCO and the composites for both gram-positive and gram-negative bacteria.

Nanoparticles	*S. aureus*		*E coli*	
	Zone of Inhibition (mm)	MIC (μg/ml)	Zone of Inhibition (mm)	MIC (μg/ml)
NZ1	12.40 ± 0.30	16	12.90 ± 0.20	16
NZ3	14.10 ± 0.20	10	13.80 ± 0.50	12
NZ5	9.50 ± 0.20	20	11.20 ± 0.50	19
ZCO	8.0 ± 0.50	23	10.10 ± 0.20	21
NiO	7.20 ± 0.30	28	9.20 ± 0.40	25

The specific capacitance of the composite was determined by utilizing equation:

$$C_{sp} = \frac{\int I\, dV}{m \times k \times \Delta V} \tag{8}$$

which factors in parameters such as the applied scan rate voltage (k), the active mass of the electrode material (m), the potential window range (Δ V), and the region beneath the CV curve as determined by the integral of the current response. The specific capacitance values obtained for the samples for different scan rates are detailed are summarized in Table S1. The highest specific capacitance of 188F/g was obtained for NZ5 for 5 mV/s.

3.4. Antibacterial activity

The results obtained from the agar well diffusion method (Fig. 6) and minimum inhibitory concentration (MIC) determination (Table-1) provide valuable insights into the antibacterial activity of the nanoparticles, warranting further discussion. Firstly, the significant bacterial growth inhibition observed for both individual and composite samples highlight the potential of the nanoparticles as effective antibacterial agents. The formation of distinct zones of inhibition surrounding the wells suggests that the nanoparticles possess inherent antimicrobial properties, which could be attributed to their chemical composition, size, and surface characteristics. The variation in MIC values among the tested nanoparticles indicates that their antibacterial efficacy varies depending on the specific composition and structure. Notably, nano-composite NZ3 exhibited the lowest MIC values, indicating its superior potency against both gram-positive (*S. aureus*) and gram-negative (*E. coli*) bacteria compared to other samples. The observed differences in antibacterial efficacy among composite nanoparticles can be attributed to factors such as composition ratio, synergistic effects between components, and nanoparticle characteristics. NZ3, with an optimized composition ratio of NiO and $ZnCo_2O_4$, exhibited the highest efficacy against both bacterial strains. The observed variability in MIC values against different bacterial strains underscores the importance of considering bacterial diversity when assessing antibacterial agents. The differences in MIC values may arise from variations in bacterial cell wall composition, membrane permeability, and susceptibility to antimicrobial agents. Understanding the underlying mechanisms of bacterial inhibition by the nanoparticles could provide valuable insights into their selective antibacterial activity. The mechanisms underlying the antibacterial activity of the nanoparticles may involve several processes, including reactive oxygen species (ROS) generation, disruption of bacterial cell membranes, release of metal ions, and surface interactions [48]. These mechanisms collectively contribute to the destabilization and eventual death of bacterial cells upon exposure to the nanoparticles.

Overall, the results suggest that the tested nanoparticles possess antibacterial properties with varying degrees of potency against different bacterial strains. These results have significant implications for the potential use of these nanoparticles in developing antimicrobial agents or coatings for various applications.

4. Conclusions

NiO and ZCO nanoparticles were synthesized using the sol-gel method, and their composite was prepared via ultrasonication. Comprehensive characterization was performed using XRD, FT-IR, and UV–Vis techniques. The composites displayed a band gap indicative of visible light transparency, while the Urbach energy values suggested the presence of disorder and imperfections. The electrical properties of the samples, including NiO, ZCO, and NiO-ZCO composites, were analyzed as a function of temperature, confirming their semiconducting nature. Electrochemical analysis revealed the charge storage capabilities of the composites, with the NZ5 composite exhibiting a specific capacitance of approximately 188 F/g as determined from CV curves. Furthermore, the antibacterial efficacy of the composites was assessed, demonstrating activity against both gram-positive and gram-negative bacteria. The NZ3 composite, in particular, showed low MIC and high ZOI values. These results suggest that these composites hold significant potential for diverse applications, including energy storage and antibacterial uses. The induced properties from composite formation indicate promising future applications in areas where spinel materials have been underutilized.

Data availability

Data will be made available on request.

CRediT authorship contribution statement

Adiba Adiba: Writing – original draft, Methodology, Investigation, Formal analysis, Data curation, Conceptualization. **Mo Ahamad Khan:** Writing – original draft, Investigation, Formal analysis, Data curation. **Tufail Ahmad:** Writing – review & editing, Validation, Supervision, Resources, Conceptualization.

Declaration of competing interest

The authors declare that they have no known competing financial interests or personal relationships that could have appeared to influence the work reported in this paper.

Acknowledgments

AA acknowledges Prof Ameer Azam, Prof Shakeel Khan, Prof Shahid Husain, and Prof Wasi Khan (AMU) for access to facilities in their labs. The authors also acknowledge USIF (AMU).

Appendix A. Supplementary data

Supplementary data to this article can be found online at https://doi.org/10.1016/j.heliyon.2024.e34880.

References

[1] T. Wang, R. Pan, M.L. Martins, J. Cui, Z. Huang, B.P. Thapaliya, C.L. Do-Thanh, M. Zhou, J. Fan, Z. Yang, M. Chi, T. Kobayashi, J. Wu, E. Mamontov, S. Dai, Machine-learning-assisted material discovery of oxygen-rich highly porous carbon active materials for aqueous supercapacitors, Nature Communications 2023 14 (1 14) (2023) 1–13, https://doi.org/10.1038/s41467-023-40282-1.

[2] A. Adiba, V. Pandey, T. Ahmad, P. Nehla, S. Munjal, Multilevel resistive switching with negative differential resistance in Al/NiO/ZnFe2O4/ITO ReRAM device, Physica B Condens Matter 654 (2023) 414742, https://doi.org/10.1016/J.PHYSB.2023.414742.

[3] O. Louafi, A. Khelef, S. Zeroual, S.E. Laouini, M.L. Tedjani, Effect of nickel nitrate concentration on the size of nickel oxide nanoparticles bio-synthesized by Artemisia herba-alba aqueous leaves extract and improving their antioxidant activities, J. Inorg. Organomet. Polym. Mater. 32 (2022) 1116–1128, https://doi.org/10.1007/S10904-021-02152-5.

[4] P. Mahajan, S. Verma, B. Padha, A. Ahmed, S. Arya, Manganese oxide and nickel oxide thin films on polyester to enable self-charging wearable supercapacitor, J. Alloys Compd. 968 (2023) 171904, https://doi.org/10.1016/J.JALLCOM.2023.171904.

[5] L.S. Eddine, H.A. Mohammed, C. Salmi, M. Souhaila, G.G. Hasan, F. Alharthi, J.A.A. Abdullah, Biogenic synthesis of Fe3O4/NiO nanocomposites using Ocimum basilicum leaves for enhanced degradation of organic dyes and hydrogen evolution, J. Porous Mater. 31 (2024) 213–226, https://doi.org/10.1007/S10934-023-01509-0.

[6] A. Aslinjensipriya, R.S. Reena, S.G. Infantiya, R. Ragu, S. Jerome Das, Probing into the physicochemical consequences of pristine and X0.06Ni0.94O (X = Co, Fe, Cu) nanoparticles for bactericidal, antifungal and hemolytic competency, J. Alloys Compd. 938 (2023) 168581, https://doi.org/10.1016/J.JALLCOM.2022.168581.

[7] M.R. Islam, M.A. Bhuiyan, M.H. Ahmed, M. Rahaman, Hydrothermal synthesis of NiO nanoparticles decorated hierarchical MnO2 nanowire for supercapacitor electrode with improved electrochemical performance, Heliyon 10 (2024) e26631, https://doi.org/10.1016/j.heliyon.2024.e26631.

[8] S.H.S. Pai, S.K. Pandey, E.J.J. Samuel, J.U. Jang, A.K. Nayak, H.S. Han, Recent advances in NiO-based nanostructures for energy storage device applications, J. Energy Storage 76 (2024) 109731, https://doi.org/10.1016/J.EST.2023.109731.

[9] S. Jayakumar, P.C. Santhosh, M.M. Mohideen, A.V. Radhamani, A comprehensive review of metal oxides (RuO2, Co3O4, MnO2 and NiO) for supercapacitor applications and global market trends, J. Alloys Compd. 976 (2024) 173170, https://doi.org/10.1016/J.JALLCOM.2023.173170.

[10] S. Li, H. Fan, Y. Yang, Y. Bi, G. Wen, L.C. Qin, Controllable synthesis of 3D hierarchical cactus-like ZnCo2O4 films on nickel foam for high-performance asymmetric supercapacitors, J. Alloys Compd. 920 (2022) 165861, https://doi.org/10.1016/J.JALLCOM.2022.165861.

[11] B. Mandal, R. Roy, P. Mitra, Fabrication of different rare earth incorporated ZnCo2O4 matrix via chemical-mechanical hybrid mechanism and study their charge carrier dynamics by Motts VRH model, J. Alloys Compd. 879 (2021) 160432, https://doi.org/10.1016/J.JALLCOM.2021.160432.

[12] M.M. Faras, S.S. Patil, P.S. Patil, A.P. Torane, Unleashing the potential of binder-free hydrothermally synthesized marigold-like ZnCo2O4 for supercapacitors, J. Energy Storage 74 (2023) 109490, https://doi.org/10.1016/J.EST.2023.109490.

[13] F. Qi, H. Li, G. Chen, S. Peng, C. Shuai, An oxygen self-supplied CuO2@g-C3N4 heterojunction endows photodynamic antibacterial performance of scaffold, J. Alloys Compd. 966 (2023) 171526, https://doi.org/10.1016/J.JALLCOM.2023.171526.

[14] W. Li, Q. You, J. Zhang, W. Li, H. Xu, Green synthesis of antibacterial LFL-ZnO using L. plantarum fermentation liquid assisted by ultrasound-microwave, J. Alloys Compd. 947 (2023) 169697, https://doi.org/10.1016/J.JALLCOM.2023.169697.

[15] L.M. Stabryla, K.A. Johnston, N.A. Diemler, V.S. Cooper, J.E. Millstone, S.J. Haig, L.M. Gilbertson, Role of bacterial motility in differential resistance mechanisms of silver nanoparticles and silver ions, Nature Nanotechnology 2021 16 (9 16) (2021) 996–1003, https://doi.org/10.1038/s41565-021-00929-w.

[16] R. Schmid, M. Volcic, S. Fischer, Z. Qu, H. Barth, A. Popat, F. Kirchhoff, M. Lindén, Surface functionalization affects the retention and bio-distribution of orally administered mesoporous silica nanoparticles in a colitis mouse model, Scientific Reports 2023 13 (1 13) (2023) 1–17, https://doi.org/10.1038/s41598-023-47445-6.

[17] J.M.V. Makabenta, A. Nabawy, C.H. Li, S. Schmidt-Malan, R. Patel, V.M. Rotello, Nanomaterial-based therapeutics for antibiotic-resistant bacterial infections, Nature Reviews Microbiology 2020 19 (1 19) (2020) 23–36, https://doi.org/10.1038/s41579-020-0420-1.

[18] D.P. Linklater, V.A. Baulin, S. Juodkazis, R.J. Crawford, P. Stoodley, E.P. Ivanova, Mechano-bactericidal actions of nanostructured surfaces, Nature Reviews Microbiology 2020 19 (1 19) (2020) 8–22, https://doi.org/10.1038/s41579-020-0414-z.

[19] V. Pandey, A. Adiba, S. Munjal, T. Ahmad, Structural and magnetic properties of tetragonal Mn3O4 nanoparticles synthesized by sol-gel method, in: AIP Conf Proc, AIP Publishing, 2020 020163, https://doi.org/10.1063/5.0001796.

[20] R. Gobi, R.S. Babu, In-vitro study on chitosan/PVA incorporated with nickel oxide nanoparticles for wound healing application, Mater. Today Commun. 34 (2023) 105154, https://doi.org/10.1016/J.MTCOMM.2022.105154.

[21] Adiba, V. Pandey, S. Munjal, T. Ahmad, Structural, morphological and magnetic properties of antiferromagnetic nickel oxide nanoparticles synthesized via sol–gel route, Mater. Today Proc. 26 (2020) 3116–3118, https://doi.org/10.1016/J.MATPR.2020.02.643.

[22] V. Pandey Adiba, S. Munjal, T. Ahmad, NiO nanoparticles: phase purification and strain analysis, AIP Conf. Proc. 2369 (2021) 020121, https://doi.org/10.1063/5.0061305.

[23] V. Pandey Adiba, S. Munjal, T. Ahmad, Structural and optical properties of sol gel synthesized NiO nanoparticles, AIP Conf. Proc. 2270 (2020) 110011, https://doi.org/10.1063/5.0020038.

[24] B.R. Jheng, P.T. Chiu, S.H. Yang, Y.L. Tong, Using ZnCo2O4 nanoparticles as the hole transport layer to improve long term stability of perovskite solar cells, Scientific Reports 2022 12 (1 12) (2022) 1–13, https://doi.org/10.1038/s41598-022-06764-w.

[25] A. Adiba, Waris, S. Munjal, M.Z. Khan, T. Ahmad, Piezo-photocatalytic degradation of organic pollutant by a novel BaTiO3–NiO composite, The European Physical Journal Plus 138 (2023) 408, https://doi.org/10.1140/epjp/s13360-023-04029-7.

[26] P. Scherrer, Bestimmung der Größe und der inneren Struktur von Kolloidteilchen mittels Röntgenstrahlen, Nachrichten von Der Gesellschaft Der Wissenschaften Zu Göttingen, Mathematisch-Physikalische Klasse (1918) 98–100, n.d. https://cir.nii.ac.jp/crid/1581417126345362048.

[27] J. Tauc, R. Grigorovici, A. Vancu, Optical properties and electronic structure of amorphous germanium, Phys. Status Solidi 15 (1966) 627–637, https://doi.org/10.1002/PSSB.19660150224.

[28] V. Pandey, Adiba, S. Munjal, T. Ahmad, Optical properties and spectroscopic investigation of single phase tetragonal Mn3O4 nanoparticles, in: Materials Today: Proceedings, Materials Today:Proceedings, 2020.

[29] M. Mao, J. Xu, J. Li, S. Zhao, X. Li, Enhancement of catalytic hydrogen evolution by NiS modification of ZnCo2O4 with cubic morphology, J. Mater. Sci. Mater. Electron. 31 (2020) 12026–12040, https://doi.org/10.1007/S10854-020-03833-6.

[30] M. Ebrahimi, V. Soleimanian, M. Ghasemi, M. Nekoeinia, A. Mokhtari, Effects of graphene quantum dots on microstructure, optical and gas sensing properties of coral-like ZnCo2O4 nanoparticles, Physica B Condens Matter 650 (2023) 414439, https://doi.org/10.1016/J.PHYSB.2022.414439.

[31] M. Stoica, C.S. Lo, P-type zinc oxide spinels: application to transparent conductors and spintronics, New J. Phys. 16 (2014) 055011, https://doi.org/10.1088/1367-2630/16/5/055011.

[32] M. Moin, A. Waheed Anwar, M. Babar, U. Thumu, A. Ali, Comparative investigations of electronic, mechanical and optical responses of Ra-doping in Barium Titanate for optoelectronic applications: a computational insight, Heliyon 10 (2024) e24607, https://doi.org/10.1016/j.heliyon.2024.e24607.

[33] K. Davis, R. Yarbrough, M. Froeschle, J. White, H. Rathnayake, Band gap engineered zinc oxide nanostructures via a sol–gel synthesis of solvent driven shape-controlled crystal growth, RSC Adv. 9 (2019) 14638–14648, https://doi.org/10.1039/C9RA02091H.

[34] A. Piyadasa, S. Wang, P.X. Gao, Band structure engineering strategies of metal oxide semiconductor nanowires and related nanostructures: a review, Semicond. Sci. Technol. 32 (2017) 073001, https://doi.org/10.1088/1361-6641/AA6778.

[35] T. Ahmad, V. Pandey, M. Saddam Husain, Adiba, S. Munjal, Structural and spectroscopic analysis of pure phase hexagonal wurtzite ZnO nanoparticles synthesized by sol-gel, Mater. Today Proc. 49 (2022) 1694–1697, https://doi.org/10.1016/j.matpr.2021.07.456.

[36] V. Pandey, A. Adiba, S. Munjal, T. Ahmad, Optical bandgap tuning of cubic spinel Co3O4 by annealing temperature, Materialia 26 (2022) 101554, https://doi.org/10.1016/j.mtla.2022.101554.

[37] Y. Fang, S. Zhang, P.R. Ohodnicki, G. Wang, Relation between cation distribution and chemical bonds in spinel NiFe2O4, Mater. Today Commun. 33 (2022) 104436, https://doi.org/10.1016/J.MTCOMM.2022.104436.

[38] T. Seki, K.Y. Chiang, C.C. Yu, X. Yu, M. Okuno, J. Hunger, Y. Nagata, M. Bonn, The bending mode of water: a powerful probe for hydrogen bond structure of aqueous systems, J. Phys. Chem. Lett. 11 (2020) 8459–8469, https://doi.org/10.1021/ACS.JPCLETT.0C01259.

[39] A. Tabet, S. Meneceur, S.E. Laouini, C. Salmi, H.A. Mohammed, I. Kir, G.G. Hasan, F. Alharthi, J.A.A. Abdullah, One post biosynthesis of novel ternary nanocomposite ZnO/CuO/Cu2MgO3 for enhancing photocatalytic degradation of bromocresol green in wastewater, J Clust Sci 35 (2024) 765–777, https://doi.org/10.1007/S10876-023-02519-3.

[40] R. Poulain, A. Klein, J. Proost, Electrocatalytic properties of (100)-, (110)-, and (111)-oriented NiO thin films toward the oxygen evolution reaction, J. Phys. Chem. C 122 (2018) 22252–22263, https://doi.org/10.1021/ACS.JPCC.8B05790.

[41] O. Farooq, M. Anis-Ur-Rehman, A. Ul Haq, Tailoring of electrical properties in nanostructured (NiO)0.25(Fe2O3)0.75 composite and compound for sensing applications, Mater. Res. Express 7 (2019) 016501, https://doi.org/10.1088/2053-1591/ab5536.

[42] D. Triyono, S.N. Fitria, U. Hanifah, Dielectric analysis and electrical conduction mechanism of La1−xBixFeO3 ceramics, RSC Adv. 10 (2020) 18323–18338, https://doi.org/10.1039/D0RA02402C.

[43] M. Ortuno, M. Pollak, The activation energy of hopping transport with sequential correlations of hops due to Coulomb interactions, J. Phys. C Solid State Phys. 16 (1983) 1459, https://doi.org/10.1088/0022-3719/16/8/015.

[44] V. Pandey, A. Adiba, P. Nehla, S. Munjal, T. Ahmad, Bipolar resistive switching with multiple intermediate resistance states in Mn3O4 thin film, Mater. Today Commun. 34 (2023) 105484, https://doi.org/10.1016/J.MTCOMM.2023.105484.

[45] X. Ji, B. Xu, H. Zhang, X. Zhang, P. Yang, NiS2 nanoparticles anchored on Co-carbon nanotubes for supercapacitor and overall water splitting, J. Alloys Compd. 968 (2023) 172192, https://doi.org/10.1016/J.JALLCOM.2023.172192.

[46] M. Yu, W. Wang, C. Li, T. Zhai, X. Lu, Y. Tong, Scalable self-growth of Ni@NiO core-shell electrode with ultrahigh capacitance and super-long cyclic stability for supercapacitors, NPG Asia Materials 2014 6 (9 6) (2014) e129, https://doi.org/10.1038/am.2014.78, e129.

[47] F. Hekmat, S. Shahrokhian, H. Hosseini, Direct growth of nickel-cobalt oxide nanosheet arrays on carbon nanotubes integrated with binder-free hydrothermal carbons for fabrication of high performance asymmetric supercapacitors, Compos. B Eng. 172 (2019) 41–53, https://doi.org/10.1016/J.COMPOSITESB.2019.05.027.

[48] M.I.A. Abdel Maksoud, G.S. El-Sayyad, N. Mamdouh, W.M.A. El Rouby, Gamma-rays induced synthesis of Ag-decorated ZnCo2O4–MoS2 heterostructure as novel photocatalyst and effective antimicrobial agent for wastewater treatment application, J. Inorg. Organomet. Polym. Mater. 32 (2022) 3621–3639, https://doi.org/10.1007/S10904-022-02387-W.